Supporting Information:

Highly Lattice-mismatched Semiconductor-Metal Hybrid Nanostructures: Gold Nanoparticle Encapsulated Luminescent Silicon Quantum Dots

Mallar Ray,[†‡]* *Tuhin Shuvra Basu,*[†‡] *Nil Ratan Bandyopadhyay,*[†] *Robert F. Klie,*[‡] *Siddhartha Ghosh,*[‡]

Sufi Oasim Raja[¥] *and Anjan Kumar Dasgupta*[¥]

[†]School of Materials Science and Engineering, Bengal Engineering and Science University, Shibpur, Howrah: 711103, West Bengal, India.

[‡] Department of Physics, University of Illinois at Chicago, Chicago 60607, Illinois, USA.

[‡] Department of Electrical and Computer Engineering, University of Illinois at Chicago, Chicago 60607, USA.

[¥]Department of Biochemistry, Calcutta University, 35 Ballygunge Circular Road, Kolkata: 700019, West Bengal, India

1. **Additional information about the structural features of HF etched Si nanostructures and the Si QD-Au NP hybrids**

Figures S1 (a)-(d) are the HRTEM images and the size distribution of freshly HF etched Si nanocrystals. The SAEDP shown as inset of Figure 1 (b) clearly shows rings of Si and the corresponding planes are (111), (220) and (311). The (331) plane is also visible (not marked). The nearly continuous rings are suggestive of random orientation of the neighboring crystallites. Figures S1 (a)-(c) reveal that there are abundant nearly spherical Si QDs whose sizes are 2 nm and below. One such free-standing spherical Si

QD is shown as the inset panel of Figure S1 (c). The log-normal distribution shown in Figure S2 (d) suggest that though the distribution spans over diameters varying from less than 1 to 4 nm, the smaller particles are more abundant than the comparatively larger ones. Hence, in an ensemble measurement the smaller particles dictate the overall behavior of the system. Such ultra-small nanocrystals of Si are expected to exhibit quantum size effects and are hence referred to as Si QDs in the paper.
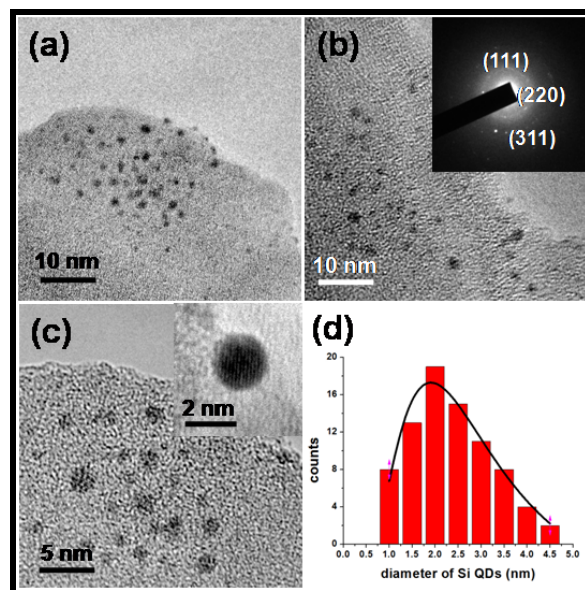

Figure S1: Bright field HRTEM images of freshly etched Si QDs showing abundant particles with diameters between ~1-4 nm (a)-(c). The inset of (b) is the SAED pattern corresponding to the bright field image, and the inset panel of (c) shows a free-standing Si QD with ~2 nm diameter. The size distribution calculated using estimated sizes of 80 particles shown in (a)-(c) exhibits a log-normal distribution (d).

To show that the dominantly achieved structures are Si-Au core-shell nanostructures some more TEM images are shown below in Figures S2 (a)-(c) which clearly demonstrate the formation of Si-Au core-shell nanostructures. It is evident from the TEM images that the Si nanostructures are indeed encapsulated by Au NPs. To illustrate the formation of Moiré fringes due to overlap of the crystalline planes of Si and Au, higher magnification images showing the formation of mixed and translational Moiré fringes due to non-accordant and accordant overlap of two crystalline mistifs are presented in Figures S2 (d) and (e),

respectively. The schematic of formation such translational and mixed Moiré patterns are illustrated in Figure S2 (f).
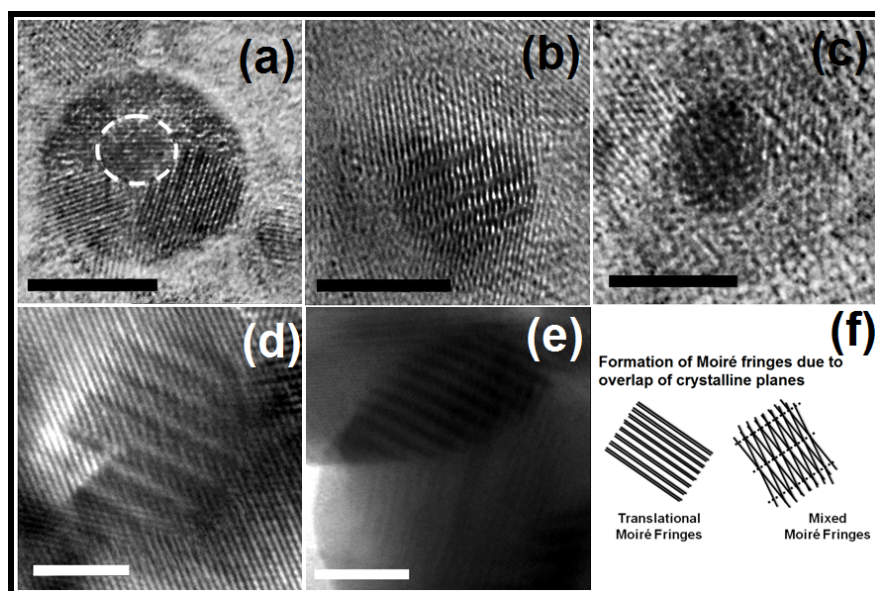

Figure S2: HRTEM images showing core-shell nanostructures Si-Au (a)-(c). Though Si has lesser contrast than Au, the formation of Moiré fringes due to overlap of the crystalline planes of Si and Au, the Si cores appear darker than the Au shells. Higher magnification images showing the formation of mixed and translational Moiré fringes due to overlap of Si and Au, are shown in (d) and (e), respectively. (f) A schematic illustrating the formation of mixed and translational Moiré fringes. The black scale bars are 5 nm and the white ones are 2 nm, respectively.

It is important to note the difficulties in simultaneously imaging Si and Au with resolvable fringes using a TEM, particularly when their feature sizes are very small. First, the shape of the envelope function severely limits the imaging of higher frequency components (i.e. smaller features in real space). This is primarily because the envelope function changes shape for different d-spacing that correspond to the possible distances between lattice fringes of nanocrystals in the image plane. In order to optimize the contrast transfer function for each spatial frequency, the defocus setting must be changed to maximize the passband for a given frequency. It is therefore difficult to simultaneously image the different planes of Si and Au having different lattice spacing. The problem becomes even more complex if there are randomly

oriented nanostructures, as it would be very difficult to simultaneously image all nanocrystals at a given focus setting. Second, in a particular image acquiring process, image settings are optimized for resolving the fringes of a single nanocrystal. This requires aligning the electron beam with the zone axis of the crystal structure under observation. For bulk crystalline material, this alignment is relatively easy because the imaging is sensitive to any deviation from the zone axis. However, for nanostructures it is very difficult to verify whether the imaging is along a zone axis.[1] Studies of Si and metal NPs have shown that resolvable lattice fringes can be achieved for a wide range of tilt angles away from the zone axis resulting in erroneous lattice spacing values.[2] The third problem associated with HRTEM imaging of individual nanocrystal is image delocalization, where fringes can extended beyond the true size of the particle. This effect can result in overestimating particle sizes and can be significant when the defocus setting is far from optimal.[3] In fact the TEM images of a two-component polymer composite NPs encapsulating Si QDs and Au NPs, reported recently,[4] were unable to confirm the presence of Si, which the authors attributed to the low scattering factor of Si. In our work, TEM imaging and analyses were done, keeping in mind the above limitations and the measured sizes (corrected up to the first decimal place) are reported only when substantive confidence could be drawn from the measurements and analyses.

Finally, it may also be noted that despite the representative images we do not claim that all the nanostructures in our sample are typical core-shell nanostructures with an Au layer surrounding the Si QD, since besides the above shown structures we could also see regions where Si QDs are apparently surrounded by Au NPs. Nevertheless, the core-shell nanostructures are indeed the dominant structures.

2. Peak assignment of the FTIR spectra:

The assignment of peaks appearing in the FTIR spectra of the Si QDs and the Au NP encapsulated Si QD hybrid were made based on the information provided in Table S1.

Table S1. Typical FTIR vibrational modes and peak positions for assignment of peaks in the FTIR spectra of different samples:

Wavenumber (cm^{-1})	Group	Mode	Reference
796	SiOSi	Bending	5
861	COC	Symmetrical Stretching	6
926	SiH$_3$	Symmetric Deformation	7
1058	SiOSi in SiO$_{1.9}$	Stretching	8
1240	C—O stretch in carboxylic acid	-	9
1403	OH in carboxylic acid	Bending	10
1566	νCOO$^-$ in acetate	Antisymmetric	11
2363	CO$_2$	-	12
3373	OH in carboxylic acid	Stretching	10

3. Reported variation of PL maxima with particle size of Si nanocrystals:

Figure S3 provides a summary of variation of PL maxima with particle size of Si nanocrystals, passivated by different ligands, extracted from few significant reports over the past two decades.

Figure R3: Reported variation of PL maxima with particle size of Si nanocrystals, passivated by different ligands, extracted from few significant reports over the past two decades (T. S. Basu, Ph.D. Thesis, BESU, Shibpur, India, 2013).
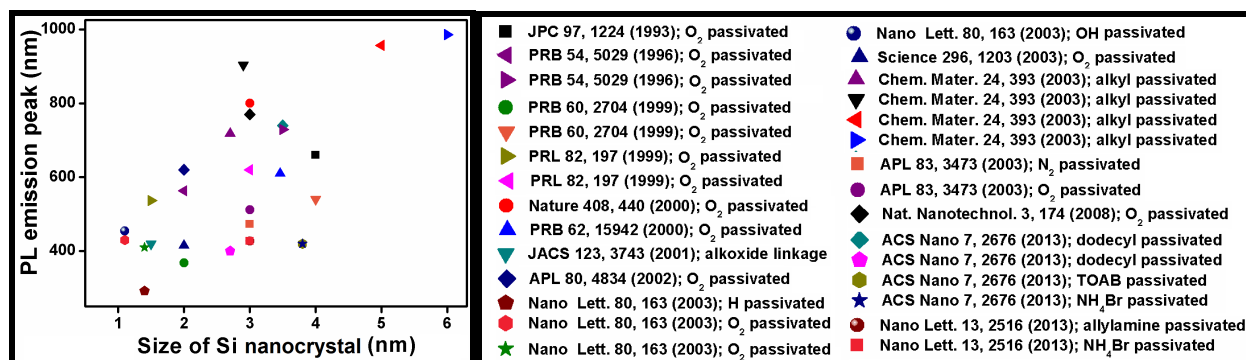
References

[1]H. Kohno, N. Ozaki, H. Yoshida, K. Tanaka, S. Takeda, Misleading fringes in TEM images and diffraction patterns of Si nanocrystallites, Crystal Research and Technology, 2003, **38**, 1082–1086.

[2] J.-O Malm, M.A O'Keefe, Deceptive "lattice spacings" in high-resolution micrographs of metal nanoparticles, Ultramicroscopy, 1997, **68**, 13-23.

[3] A. Ziegler, C. Kisielowski, R. O. Ritchie, Imaging of the crystal structure of silicon nitride at 0.8 Ångström resolution, Acta Mater. 2002, **50**, 565-574.

[4] N. A. Harun, M. J. Benning, B. R. Horrocks, and D. A. Fulton, Gold nanoparticle-enhanced luminescence of silicon quantum dots co-encapsulated in polymer nanoparticles, Nanoscale, 2013, **5**, 3817.

[5] S. Hayashi, S. Tanimoto, and K. Yamamoto, Analysis of surface oxides of gas-evaporated Si small particles with infrared spectroscopy, high-resolution electron microscopy, and x-ray photoemission spectroscopy, J. Appl. Phys. 1990, **68**, 5300-5308.

[6] J. G. V. Soest, H. Tournois, D. D. Wit, and J. J. G. Vliegenthat, Short-range structure in (partially) crystalline potato starch determined with attenuated total reflectance Fourier-transform IR spectroscopy, Carbohydrate Res. 1995, **279** 201—214

[7] I. V. Kochikov, G. M. Kuramshina, S. V. Syn'ko, and Y. A. Pentin, Normal coordinate analysis of CH_2ClSiX_3, $CHCl_2SiX_3$, CCl_3SiX_3 (X = H, D, F, Cl) Molecules using Tikhonov's regularization method, J. Mol. Struct. 1988, **172**, 299.

[8] P. G. Pai, S. S. Chao, Y. Takagi, and G. Luckovosky, Infrared spectroscopic study of SiO_x films produced by plasma enhanced chemical vapor deposition J. Vac. Sci. Technol. A 1986, **4,** 689.

[9] E. Smidt, K. U. Eckhardt, P. Lechner, H. R. Schulten, and P. Leinweber, Characterization of different decomposition stages of biowaste using FT-IR spectroscopy and pyrolysis-field ionization mass spectrometry, Biodegradation. 2005, **16,** 67-79.

[10] O. Gershevitz and C. N. Sukenik, In situ FTIR-ATR analysis and titration of carboxylic acid-terminated SAMs, .J. Am. Chem. Soc. 2004, **126**, 482.

[11] P. Sazama, L. Capek, H. Drobná, Z. Sobalík, J. Dědeček, K. Arve, B. Wichterlová, Enhancement of decane-SCR-NO_x over Ag/alumina by hydrogen. Reaction kinetics and in situ FTIR and UV–vis study, J. Catal. 2005, **232**, 302-317.

[12]B. C. Smith, Fundamentals of Fourier transform infrared spectroscopy, CRC Press, Florida, USA 1996.